

Finite-difference simulations of transient radiation from a finite-length pipe

Daniel R. Tengelsen^{a)}

Acoustics Research Group, Department of Physics and Astronomy, Brigham Young University, Provo, Utah 84602

Brian E. Anderson^{b)}

Geophysics Group (EES-17), MS D446, Los Alamos National Laboratory, Los Alamos, New Mexico 87545

Vianey Villamizar

Department of Mathematics, Brigham Young University, Provo, Utah 84602

Timothy W. Leishman

Acoustics Research Group, Department of Physics and Astronomy, Brigham Young University, Provo, Utah 84602

(Received 14 January 2013; revised 21 September 2013; accepted 8 November 2013)

The far-field radiation originating from a finite-length pipe is well studied, especially for steady-state conditions. However, because all physical systems do not begin in steady state, these radiation characteristics are only valid after the transient portion of the solution has decayed. Understanding transient radiation characteristics may be important (particularly for systems transmitting very short-duration signals), as they can differ quite significantly. A numerical complication to this problem involves dealing with a sharp corner in the domain of interest. While many numerical studies have attempted to couple solutions from the domains inside and outside a pipe, the analysis presented in this work treats the computational domain as a single region by expressing the entire physical domain as a map from a simple rectangular domain in generalized curvilinear coordinates. This method will be introduced in detail and general results of transient radiation will be presented for an infinitely baffled, finite-length pipe using the finite-difference method expressed in generalized curvilinear coordinates. Comparison will be made to previous results [P. Stepanishen and R. A. Tougas, *J. Acoust. Soc. Am.* **93**, 3074–3084 (1993)] that used a semi-analytic approach with certain assumptions. © 2014 Acoustical Society of America. [<http://dx.doi.org/10.1121/1.4835915>]

PACS number(s): 43.20.Px, 43.20.Mv, 43.20.Ei [NAG]

Pages: 17–26

I. INTRODUCTION

Wave propagation through and from a pipe is a widely studied topic in acoustics. Many researchers interested in turbomachinery, ventilation systems, mufflers, exhaust pipes, loudspeakers, etc., use the analysis of this system as a first step to better understand more-complicated systems of interest.^{1–5} Additionally, the problem has been posed several different ways in the past, rendering it broad and diverse in both its solutions and applications. For example, pipes of finite, semi-infinite, and infinite lengths with both baffled and unbaffled ends and of constant or varying cross-section have been studied analytically, numerically, and experimentally. Furthermore, both time-harmonic^{1,5–14} and transient^{2–4,15} source conditions have been investigated.

The most applicable work to this paper is that of Stepanishen and Tougas, who semi-analytically approximated the transient radiation from a baffled, finite-length pipe for a short-duration signal.¹⁵ Their analysis assumed the

pipe to be circularly symmetric and the problem was solved via transform methods, where the field variable for both a circular pipe and a half space were matched at the adjoining boundary. Their study investigated the radiation characteristics of several modes generated within the pipe and showed that radiation from higher-order pipe modes produced no on-axis pressure in the far field. In order to simplify the analytical complexities of matching the tractable solutions for both the pipe and half-space domains, there was an assumed one-to-one correspondence between the pipe modes that composed the incident pressure wave propagating toward the pipe exit and the reflected pressure wave propagating back down the pipe. For example, a plane wave impinging on the pipe exit would only produce a plane wave upon reflection back down the pipe. These authors clearly noted the simplification involved in having a one-to-one correspondence between incident and reflected pipe modes, and they concluded their work by stating that this assumption would need to be studied in further detail.

In this work, we introduce a relatively new development for the finite-difference method (FDM), which involves numerically mapping a simple rectangular domain, expressed in generalized curvilinear coordinates, to a more complicated or irregular geometry in Cartesian coordinates. We demonstrate the basic process required, which involves

^{a)}Current address: Applied Research Laboratories, 10000 Burnet Rd., F0270, Austin, TX 78758.

^{b)}Author to whom correspondence should be addressed. Electronic mail: bea@lanl.gov

moving the analytical equations into a generalized curvilinear domain and Taylor expanding the differentials to create the finite-difference problem. We contrast this approach with other more conventional mapping techniques. The numerical simulations for this study employ a second-order, leapfrog-type FDM to evaluate time-domain wave propagation for short-duration transient signals.

We demonstrate the robust nature of this grid-generation technique by considering the problem solved semi-analytically by Stepanishen and Tougas; this geometry contains a sharp edge wherein the pipe exit joins the half space, making it a more problematic geometry for conventional software packages (i.e., see discussion at the end of Sec. II C). By reproducing this problem numerically, the two domains (the pipe and the half space) become a single domain, thus eliminating the need for their simplification and allowing us to quantify its validity. Additionally, by including a half space in the grids used to simulate wave propagation, we eliminate the need to define a complicated impedance boundary condition at the pipe exit. As with the work of Stepanishen and Tougas, the pipe is assumed rigid and the case of no mean flow is considered. Some higher-order modes are also independently excited in this initially quiescent field by a single-cycle, gated sine wave. Last, this problem is reproduced using COMSOL, a standard finite-element software package, to both verify and compare against the results from the method presented here.

II. THE MATHEMATICAL PROBLEM

A. The physical problem

Transient radiation is studied from a finite-length pipe mounted to an infinite rigid baffle. At time $t=0$, the fluid is excited at the end of the pipe not mounted to the baffle. The excitation signal is defined as a gated, single-cycle sine wave. Once excited, an acoustic wave propagates through the pipe and eventually radiates to infinity within a half-space domain.

Inside the pipe and in the half space outside the pipe, the sound pressure p is mathematically modeled by the wave equation in cylindrical coordinates (r, ϕ, z) , where we assume the field to be independent of ϕ :

$$\frac{\partial^2 p}{\partial r^2} + \frac{1}{r} \frac{\partial p}{\partial r} + \frac{\partial^2 p}{\partial z^2} = \frac{1}{c_0^2} \frac{\partial^2 p}{\partial t^2}. \quad (1)$$

The radial coordinate r is perpendicular to the normal of the infinite baffle, the z coordinate is parallel with the pipe, and c_0 is the free-field sound speed of the fluid. An illustration of the physical problem is given in Fig. 1. The right-hand illustration in Fig. 2 depicts the computational interpretation of the physical domain D , where wave propagation is numerically simulated with the grid. Its boundaries $C_1 \cup C_2 \cup C_3 \cup C_4$ are also illustrated.

The boundary condition at C_4 models a rigid condition for both the pipe wall and the infinite baffle. At C_3 , the symmetry condition requires that the pressure is continuous,

$$\lim_{\epsilon \rightarrow 0} p(\epsilon, z, t) = p(-\epsilon, z, t), \quad (2)$$

which leads to the boundary condition

$$\frac{\partial}{\partial r} p(0, z, t) = 0. \quad (3)$$

The condition on C_1 is defined by the nature of the excitation at this end of the pipe. It is assumed that the pressure field is initially quiescent. Also, the mathematical description of the outgoing wave at infinity is given through the well-known Sommerfeld radiation condition, $p_t + c_0 p_R \rightarrow 0$ as $R \rightarrow \infty$, where the subscripts t and R , respectively, denote derivatives in time and space where $R = \sqrt{x^2 + y^2 + z^2}$ with its origin at the center of the pipe exit.

Because this initial boundary-value problem (IBVP) is solved numerically for p using the FDM in generalized curvilinear coordinates to account for irregular geometries, a truncation of the infinite half space to the right of the pipe is necessary. Thus, the boundary C_2 shown in the right-hand illustration of Fig. 2 corresponds to an artificial infinite boundary. This requires an introduction of an absorbing condition at C_2 instead of the Sommerfeld radiation condition. This condition should be such that there are no spurious reflections at the absorbing boundary. In this work, the radiation condition $p_t + c_0 p_R + (c_0/2R)p \rightarrow 0$, as $R \rightarrow \infty$ of $\mathcal{O}(1/R^{5/2})$ is used. A complete review of the non-reflecting boundary condition used in this paper is given by Bayliss *et al.* and Givoli.^{16–18} Summarily, the IBVP in complete mathematical form is expressed as

$$\frac{1}{c_0^2} p(r, z, t)_{tt} = p_{rr} + \frac{1}{r} p_r + p_{zz}, \quad (r, z) \in \mathcal{D}, t > 0, \quad (4)$$

$$\frac{\partial}{\partial n} p(r, z, t) = 0 \quad (r, z) \in C_4 \cup C_3, \quad (5)$$

$$\frac{\partial}{\partial n} p(r, z, t) = \begin{cases} -\rho_0 \hat{a}(r, t), & 0 \leq t \leq T_d, \\ 0, & \text{otherwise,} \end{cases} \quad (r, z) \in C_1, \quad (6)$$

$$p_t + c_0 p_R + \frac{c_0}{2R} p = 0, \quad (r, z) \in C_2, \quad (7)$$

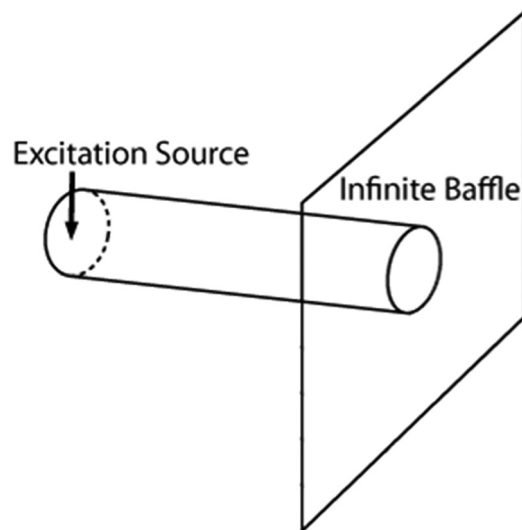


FIG. 1. Illustration of the physical domain used to study transient radiation from a finite-length pipe.

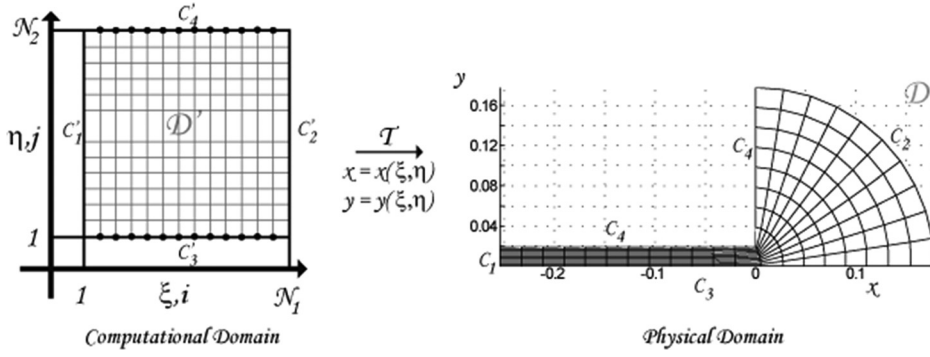


FIG. 2. Illustration of the transformation used in the generation of boundary-conforming coordinates.

$$p(r, z, 0) = 0 \quad \text{and} \quad p_t(r, z, 0) = 0, \quad (r, z) \in D. \quad (8)$$

B. The physical problem in generalized curvilinear coordinates

Since much of the work done in generalized curvilinear coordinates (ξ and η) maps to or from Cartesian coordinates (x and y), it is desirable to write this IBVP in terms of x and y . Since the wave equation no longer depends on ϕ , the variables r and z are easily identified with y and x , respectively. Thus, choosing $y = r$ and $x = z$, Eq. (4) can be written as

$$\frac{\partial^2 p}{\partial y^2} + \frac{1}{y} \frac{\partial p}{\partial y} + \frac{\partial^2 p}{\partial x^2} = \frac{1}{c_0^2} \frac{\partial^2 p}{\partial t^2}, \quad (9)$$

where p is now written as a function of x , y , and t .

The mapping to curvilinear coordinates can be mathematically described by a transformation to generalized curvilinear coordinates (ξ, η) from Cartesian coordinates (x, y) [though it should be remembered that our equation employs cylindrical coordinates ($z = x, r = y$)]. Figure 2 pictorially describes this transformation $T: \mathcal{D}' \rightarrow \mathcal{D}$, defined by $x = x(\xi, \eta)$ and $y = y(\xi, \eta)$ from a rectangular region \mathcal{D}' called the computational domain to the plane region \mathcal{D} called the physical domain.

As a result, the pressure is written in terms of curvilinear coordinates as $p(\xi, \eta) = p(x(\xi, \eta), y(\xi, \eta))$. Moreover, the wave equation expressed in Eq. (9) transforms into

$$\begin{aligned} & \frac{1}{J^2} (\alpha p_{\xi\xi} - 2\beta p_{\xi\eta} + \gamma p_{\eta\eta}) + \frac{1}{J^3} (\alpha y_{\xi\xi} - 2\beta y_{\xi\eta} + \gamma y_{\eta\eta}) (x_{\eta} p_{\xi} - x_{\xi} p_{\eta}) + \frac{1}{J^3} (\alpha x_{\xi\xi} - 2\beta x_{\xi\eta} + \gamma x_{\eta\eta}) (y_{\xi} p_{\eta} - y_{\eta} p_{\xi}) \\ & + \frac{1}{yJ} (x_{\xi} p_{\eta} - x_{\eta} p_{\xi}) = \frac{1}{c_0^2} p_{tt}, \end{aligned} \quad (10)$$

in generalized curvilinear coordinates, where subscripts denote partial derivatives and $\alpha = x_{\eta}^2 + y_{\eta}^2$, $\beta = x_{\xi} x_{\eta} + y_{\xi} y_{\eta}$, $\gamma = x_{\xi}^2 + y_{\xi}^2$, and $J = x_{\xi} y_{\eta} - x_{\eta} y_{\xi}$, which corresponds to the Jacobian of the transformation.

The mathematical transformation T between coordinate systems, introduced by Villamizar and Acosta, is adopted,¹⁹

$$\alpha x_{\xi\xi} - 2\beta x_{\xi\eta} + \gamma x_{\eta\eta} = -\alpha\psi(\xi, \eta)x_{\xi} - \gamma\phi(\xi, \eta)x_{\eta}, \quad (11)$$

$$\alpha y_{\xi\xi} - 2\beta y_{\xi\eta} + \gamma y_{\eta\eta} = -\alpha\psi(\xi, \eta)y_{\xi} - \gamma\phi(\xi, \eta)y_{\eta}, \quad (12)$$

where $\psi = \alpha_{\xi}/2\alpha$ and $\phi = \gamma_{\eta}/2\gamma$ are known as grid control functions. A more conventional conformal map was first introduced by Winslow,²⁰ which uses the same equations given in Eqs. (11) and (12) but without the grid control

functions. While these types of grids are generally smooth, a lack of grid control functions provides no control over the location of the grid lines. As a consequence, these grids often contain vast differences in cell size, creating computational instabilities, and/or numerical inaccuracies. Because of the sharp corner in the geometry used for this study, the grid control functions allow for a more uniform cell size, while maintaining the desirable feature of near orthogonal grids, which is common to most elliptic grid generators. (Recent work involving grid line control can be found in books by Hansen *et al.*²¹ and Thompson *et al.*²²) Thus, substitution of Eqs. (11) and (12) into Eq. (10) simplifies the expression considerably. Once again, the entire IBVP is presented, but written in terms of generalized curvilinear coordinates:

$$\frac{1}{J^2} (\alpha p_{\xi\xi} - 2\beta p_{\xi\eta} + \gamma p_{\eta\eta}) + \left(\frac{\alpha\psi}{J^2} - \frac{x_{\eta}}{yJ} \right) p_{\xi} + \left(\frac{\gamma\phi}{J^2} + \frac{x_{\xi}}{yJ} \right) p_{\eta} = \frac{1}{c_0^2} p_{tt}, \quad (\xi, \eta) \in \mathcal{D}', \quad t > 0, \quad (13)$$

$$\frac{\partial}{\partial n} p(\xi, \eta, t) = \frac{1}{J\sqrt{\gamma}} (\gamma p_{\eta} - \beta p_{\xi}) = 0, \quad (\xi, \eta) \in C_4 \cup C_3, \quad (14)$$

$$\frac{\partial}{\partial n} p(\zeta, \eta, t) = \frac{1}{J\sqrt{\alpha}} (\beta p_\eta - \alpha p_\xi) = \begin{cases} -\rho_0 \hat{a}(\eta, t), & 0 \leq t \leq T_d, \\ 0, & \text{otherwise,} \end{cases} \quad (\zeta, \eta) \in C'_1, \quad (15)$$

$$p_t + \frac{c_0}{JR} [(xy_\eta - yx_\eta)p_\xi + (yx_\xi - xy_\xi)p_\eta] + \frac{c_0}{2R} p = 0, \quad (\zeta, \eta) \in C'_2, \quad (16)$$

$$p(\zeta, \eta, 0) = 0 \quad \text{and} \quad p_t(\zeta, \eta, 0) = 0, \quad (\zeta, \eta) \in \mathcal{D}', \quad (17)$$

where R (due to the coordinate/variable changes) is now calculated by $\sqrt{x^2 + y^2}$. Equations (13) through (17) are in the form used during the finite-difference (FD) simulation and must therefore be discretized, as described in the following section.

C. Discretization

A second-order discretization of all the governing equations expressed in curvilinear coordinates is needed for the FD simulations. Since the governing equations are partial differential equations in time and space, discretization must occur both temporally and spatially. Temporally, the compu-

tation requires the current and past time steps to infer what the solution of the governing equation over the computational domain will be in the future. This second-order method is similar to the leapfrog scheme. Time steps are indicated with the index n and written as superscripts in the following equations. Spatially, the computational domain \mathcal{D}' is described by the coordinates ζ and η , where $1 \leq \zeta \leq N_1$ and $1 \leq \eta \leq N_2$. For convenience, the computational step size for both of these coordinates is $\Delta\zeta = \Delta\eta = 1$. The spatial step numbers are indicated with the subscripts i and j , which correspond to steps taken in ζ and η , respectively.

By using the following spatial and temporal discretizations,

$$\begin{aligned} p_{tt} &= p_{i,j}^{n+1} - 2p_{i,j}^n + p_{i,j}^{n-1}, & p_\eta &= (p_{i,j+1}^n - p_{i,j-1}^n)/2, \\ p_{\xi\xi} &= p_{i+1,j}^n - 2p_{i,j}^n + p_{i-1,j}^n, & (x_\eta)_{i,j} &= (x_{i,j+1} - x_{i,j-1})/2, \\ p_{\xi\eta} &= (p_{i+1,j+1}^n - p_{i+1,j-1}^n - p_{i-1,j+1}^n + p_{i-1,j-1}^n)/4, & (x_\xi)_{i,j} &= (x_{i+1,j} - x_{i-1,j})/2, \\ p_{\eta\eta} &= p_{i,j+1}^n - 2p_{i,j}^n + p_{i,j-1}^n, & (y_\eta)_{i,j} &= (y_{i,j+1} - y_{i,j-1})/2, \\ p_\xi &= (p_{i+1,j}^n - p_{i-1,j}^n)/2, & (y_\xi)_{i,j} &= (y_{i+1,j} - y_{i-1,j})/2, \end{aligned}$$

we solve for the pressure at the future time step. Thus, the wave equation in curvilinear coordinates [Eq. (13)] becomes

$$\begin{aligned} p_{i,j}^{n+1} &= 2p_{i,j}^n - p_{i,j}^{n-1} \\ &+ \delta_{i,j}^2 [\alpha_{i,j} (p_{i+1,j}^n - 2p_{i,j}^n + p_{i-1,j}^n) \\ &- \frac{\beta_{i,j}}{2} (p_{i+1,j+1}^n - p_{i+1,j-1}^n - p_{i-1,j+1}^n + p_{i-1,j-1}^n) \\ &+ \gamma_{i,j} (p_{i,j+1}^n - 2p_{i,j}^n + p_{i,j-1}^n) \\ &+ \left(\frac{(\alpha_\xi)_{i,j}}{4} - \frac{J_{i,j}(x_\eta)_{i,j}}{2y_{i,j}} \right) (p_{i+1,j}^n - p_{i-1,j}^n) \\ &+ \left(\frac{(\gamma_\eta)_{i,j}}{4} + \frac{J_{i,j}(x_\xi)_{i,j}}{2y_{i,j}} \right) (p_{i,j+1}^n - p_{i,j-1}^n)], \quad (18) \end{aligned}$$

where $\delta_{i,j} = c_0 \Delta t / J_{i,j}$ and Δt is the time step.

Equation (18) is only used to calculate $p_{i,j}^{n+1}$ on the interior points of the computational domain. In order to compute an edge of this domain, the boundary condition equations [Eqs. (14)–(17)] need to be discretized. Accurate

computations at the boundaries require the consideration of ghost points. These are points that lie outside of the domain, but can still be used in the calculation of the field values at the boundary points. Essentially, the ghost points provide the additional grid points needed to combine the governing equation [Eq. (18)] with the discretized boundary-condition equations. This combination of equations is desirable so that field values at boundary points incorporate both wave motion and the boundary stipulations.

Since the discretizations of the boundary conditions are different for each boundary of the domain, they are treated individually. At the boundary line C_1 , second-order discretization gives

$$p_{0,j}^n = \begin{cases} p_{2,j}^n - \left[\frac{\beta_{1,j}}{\alpha_{1,j}} (p_{1,j+1}^n - p_{1,j-1}^n) + \frac{2\rho_0(\hat{a})_{1,j}}{\alpha_{1,j}} \right], & 0 \leq t \leq T_d, \\ p_{2,j}^n - \frac{\beta_{1,j}}{\alpha_{1,j}} (p_{1,j+1}^n - p_{1,j-1}^n), & \text{otherwise,} \end{cases} \quad (19)$$

where the value at the ghost point $p_{0,j}^n$ is now determined. Once the field value at the ghost point is calculated, substitution of this value into Eq. (18) gives the pressure field at that boundary point. As mentioned previously, the boundary conditions are thus correctly accounted for in the governing equation via substitution of the ghost point.

The rigid condition on boundary C_4 and the symmetry condition on boundary C_3 are very similar. Both require that the normal derivative of the pressure be zero. Their discretizations are similar since their normal vectors are in the same axis (but opposite in direction) in the *computational* domain. Once again, second-order discretizations and ghost points are used to calculate the field values at these boundaries. Thus,

$$p_{i,N_2+1}^n = p_{i,N_2-1}^n + \frac{\beta_{i,N_2}}{\gamma_{i,N_2}} (p_{i+1,N_2}^n - p_{i-1,N_2}^n), \quad (20)$$

which solves for the ghost points just outside boundary C_4 , and

$$p_{i,0}^n = p_{i,2}^n, \quad (21)$$

which solves for the ghost points for boundary C_3 . Both sets of ghost points are then substituted into Eq. (18) to calculate the pressure field on each respective boundary.

Finally, a second-order discretization of the absorbing boundary condition on boundary C_2 is presented. Because both the governing wave equation and the absorbing boundary condition contain derivatives of pressure both temporally and spatially, finding $p_{N_1,j}^{n+1}$ requires that both equations be first solved in terms of the ghost point $p_{N_1+1,j}^n$. Then both discrete equations are set equal to one another, eliminating this ghost point and resulting in a single equation for the future pressure value at the boundary $p_{N_1,j}^{n+1}$. This procedure produces the following equation, given without derivation:

$$p_{N_1,j}^{n+1} = \frac{1}{1 + \frac{c_0 \Delta t R}{\lambda_{N_1,j} J_{N_1,j}} \left(\alpha_{N_1,j} + \frac{(\alpha_\xi)_{N_1,j}}{4} - \frac{(x_\eta)_{N_1,j} J_{N_1,j}}{2y_{N_1,j}} \right)} \times \left\{ \delta_{N_1,j}^2 \left[\left(\alpha_{N_1,j} + \frac{(\alpha_\xi)_{N_1,j}}{4} - \frac{(x_\eta)_{N_1,j} J_{N_1,j}}{2y_{N_1,j}} \right) \left(-\frac{2\kappa_{N_1,j}}{\lambda_{N_1,j}} p_\eta - \frac{J_{N_1,j}}{\lambda_{N_1,j}} p_{N_1,j}^n + \frac{R J_{N_1,j}}{c_0 \lambda_{N_1,j} \Delta t} p_{N_1,j}^{n-1} \right) + 2\alpha_{N_1,j} (p_{N_1-1,j}^n - p_{N_1,j}^n) - 2\beta_{N_1,j} p_{\xi\eta} + \gamma_{N_1,j} p_{\eta\eta} + \left(\frac{(\gamma_\eta)_{N_1,j}}{2} + \frac{(x_\xi)_{N_1,j} J_{N_1,j}}{y_{N_1,j}} \right) p_\eta \right] + 2p_{N_1,j}^n - p_{N_1,j}^{n-1} \right\}, \quad (22)$$

where $\kappa_{N_1,j} = y_{N_1,j} (x_\xi)_{N_1,j} - x_{N_1,j} (y_\xi)_{N_1,j}$ and $\lambda_{N_1,j} = x_{N_1,j} (y_\eta)_{N_1,j} - y_{N_1,j} (x_\eta)_{N_1,j}$.

In summary, an FD technique has now been developed, supported by a set of special elliptic grids, which applies to wave propagation through axially symmetric boundaries in three-dimensional space. The grid control functions α and ϕ introduced in Eqs. (11) and (12) aid in creating a more uniform cell area, while also enhancing smoothness and orthogonality.²³ While others have introduced usable techniques for improving grid generation on complex structures,^{20–22} the grid-generation technique given here is fully automatic,²³ more stable,²⁴ and has even been shown to outperform grids created by ANSYS (a popular computer-aided engineering software package) when including a sharp corner.¹⁹ Villamizar and Acosta have continued to develop a variety of curvilinear grids, similar to that used here, and have applied them to scattering from multiple nonconventional objects in two-dimensions.^{24,25}

III. NUMERICAL SIMULATION

The model simulated in this work is scaled down to exactly $\frac{1}{4}$ the size of the mathematical model used by Stepanishen and Tougas.¹⁵ Thus, their 4 kHz results correspond to the 16 kHz results presented here. The cylindrical,

rigid pipe for this model is 0.5 m long with a radius of $r_a = 19.05$ mm (0.75 in.), where one end of the pipe is mounted to an infinite, rigid baffle.

The absorbing boundary condition at C_2 was applied at a constant radius $R = 50$ cm from the origin (the center of the pipe exit), over 7.5 times the Rayleigh distance $kr_a^2/2$, where k is the acoustic wave number for the highest frequency of interest. The reflection coefficient from this boundary was calculated to be approximately 1%.²⁶ Moving it to distances of 80 and 100 cm from the pipe exit and measuring the field values at the same positions did create some slight differences in the radiation patterns versus angle. However, the differences were likely due to the superposition of the small reflected pressure waves from the absorbing boundary. Therefore, a valuable comparison to Stepanishen and Tougas' far-field results can still be made. Because it was of computational interest to keep the grid small and because the results were still comparable, the boundary was kept at the 50 cm distance.

An appropriate acceleration profile was defined to independently excite natural modes of the pipe. The goal was to create a source function that enabled all of the acoustic energy produced by the source to be transferred into any desired mode. Following Stepanishen and Tougas, the acceleration profile of the piston $\hat{a}(r, t)$ satisfied the following relationship:

$$\alpha_{m,n} = \frac{1}{S} \int_S \hat{a}(r,t) \Phi_{m,n} dS, \quad (23)$$

where $\alpha_{m,n}$ is the m,n th modal amplitude coefficient (differing from the grid metric α used above), $\Phi_{m,n}$ is the m,n th mode (eigenfunction) of a circular pipe, and S is the cross-sectional area of the pipe. For a circularly symmetric pipe, these eigenfunctions are

$$\Phi_{0,n} = J_0(\chi_{0,n}r), \quad n = 1, 2, \dots, \quad (24)$$

where $J_0(\chi_{0,n}r)$ is a zero-order Bessel function of the first kind. Subscript m is always zero because only axisymmetric modes are considered, as was done by Stepanishen and Tougas. The values of $\chi_{0,n}$ are determined from the rigid boundary condition at the pipe radius, $r = r_a$, and are the set of discrete values satisfying the wave equation in the radial direction. Thus, substitution of Eq. (24) into Eq. (23) results in the expression

$$\alpha_{0,n} = \frac{1}{S} \int_S \hat{a}(r,t) \Phi_{0,n} dS = \frac{2\pi}{S} \int_0^{r_a} \hat{a}(r,t) J_0(\chi_{0,n}r) r dr. \quad (25)$$

In order to independently excite the n th mode of the pipe, we choose the profile to be

$$\hat{a}(r,t) = \begin{cases} J_0(\chi_{0,p}r) \sin\left(\frac{2\pi t}{T_d}\right), & 0 \leq t \leq T_d, \\ 0, & \text{otherwise,} \end{cases} \quad (26)$$

where T_d is the period of the single-cycle sine wave. The spatial nature of this profile is convenient due to the orthogonality property of the Bessel function for $0 \leq t \leq T_d$,

$$\begin{aligned} \alpha_{0,n} &= \frac{2\pi}{S} \int_0^{r_a} J_0(\chi_{0,p}r) \sin\left(\frac{2\pi t}{T_d}\right) J_0(\chi_{0,n}r) r dr \\ &= \begin{cases} J_0(\chi'_{1,p})^2 \sin\left(\frac{2\pi t}{T_d}\right), & p = n, \\ 0, & p \neq n, \end{cases} \end{aligned} \quad (27)$$

where $\chi'_{1,n}$ is the n th root of the first-order Bessel function of the first kind.²⁷ This spatial profile is the simplest that can be chosen to independently excite a pipe mode.

IV. RESULTS

The FD model allows the study of the angular and time-dependent properties of each natural mode of the pipe as they subsequently radiate to the absorbing boundary C_2 . As explained in the previous section, the acceleration profile at the source boundary is prescribed spatially as a Bessel function of the first kind of order zero for independent modal excitation. Simulations of the first three modes of the pipe, independently excited and radiated to the absorbing boundary, were recorded and analyzed using a 3101×71 point grid. The transient nature of the signal induced significant numerical dispersion and therefore necessitated an extremely fine grid to account for the high-frequency content of the

pulse. It permitted frequencies slightly higher than 52 kHz, assuming 20 grid points per wavelength. Sufficient grid resolution was verified by refining the grid until the (0,0) natural mode propagated through the pipe without visually obvious dispersion. This same check was also performed with the data received at the absorbing boundary, as the element sizes are larger here than in the pipe. In addition, other works have discussed this issue in more detail for similar problems.²⁸ Figure 3(d) shows the negligible amount of numerical dispersion for the chosen grid resolution while the sound is radiated through the pipe. Finally, computation time for each simulation was approximately 37 min when run on a dual-core 32-bit computer with a 3.16 GHz processor and coded in MATLAB. The step size was set to be approximately $\Delta t = 2 \times 10^{-7}$ s.

Figures 3 and 4 show the development of wave propagation over time for the plane-wave and the first higher-order mode, respectively, and a 16 kHz single-cycle sinusoidal excitation. For the plane-wave mode, the pulse begins and remains as a compact compression. However, for the first higher-order mode, the signal rapidly disperses as the energy created by the pulse travels down the pipe at many different speeds. This is explained by phase and group speeds in many fundamental acoustics textbooks.^{27,29} Lower-order modes travel down the pipe faster than higher-order modes for a given non-infinite frequency, and higher frequencies travel down the pipe faster than lower frequencies for a given non-planar mode.

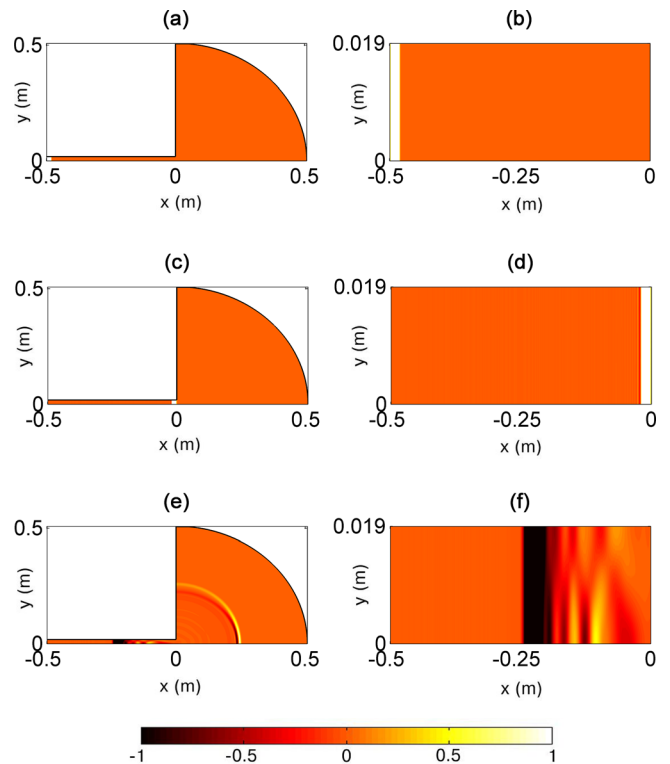


FIG. 3. (Color online) Wave propagation images (spatial distribution of pressure at an instant in time) for a single-cycle 16 kHz excitation signal in the (0,0) mode. Wave propagation for the full spatial model is shown to scale in (a), (c), and (e). Wave propagation solely within the pipe is shown in (b), (d), and (f). The times for each subplot are as follows: (a) and (b) 0.0625 ms, (c) and (d) 1.5 ms, (e) and (f) 2.2 ms.

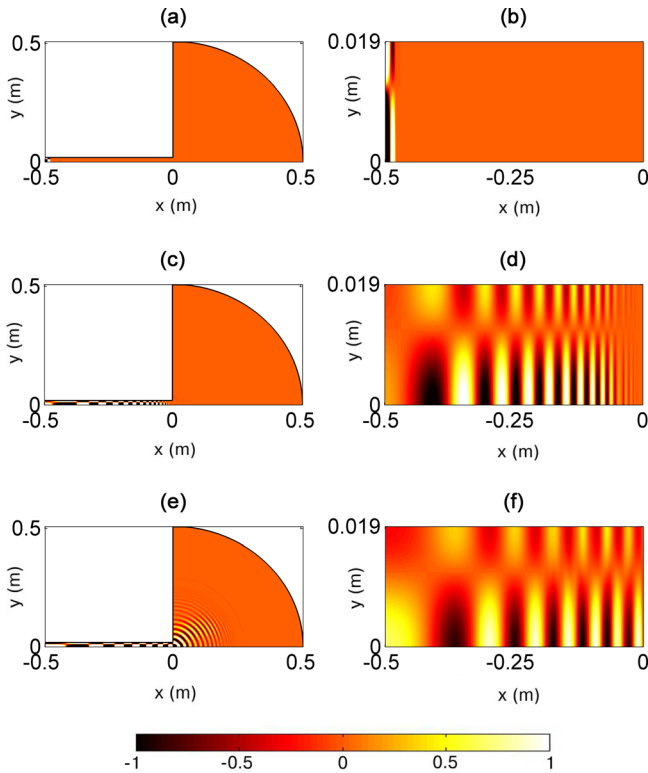


FIG. 4. (Color online) Wave propagation images (spatial distribution of pressure at an instant in time) for a single-cycle 16 kHz excitation signal in the (0,1) mode. Wave propagation for the full spatial model is shown to scale in (a), (c), and (e). Wave propagation solely within the pipe is shown in (b), (d), and (f). The times for each subplot are as follows: (a) and (b) 0.0625 ms, (c) and (d) 1.5 ms, (e) and (f) 2.2 ms.

While it is important to keep this fundamental analysis in mind, many physical systems will likely never be this simple. Many sources cannot produce just one mode independently; their radiating surfaces commonly break up into higher-order structural modes in an attempt to reproduce high frequencies, thus exciting many different modes. Consequently, some low-frequency energy may be imparted to the plane-wave mode, which allows low-frequency energy to be found at the front of the transient pulse as it propagates down the pipe. In the literature, one related physical experiment involved a ceramic disk as the excitation source.³ The spread of frequencies was reported such that low frequencies traveled down the pipe faster than higher frequencies and could, with a long enough pipe, spread out enough to produce an audible frequency sweep.

Another phenomenon related to frequency shifts, reported by Stepanishen and Tougas, is that the system sweeps down in frequency after the initial signal is radiated into the far field.¹⁵ The observation that higher frequencies radiate from pipes more easily is consistent with theory. Because their wavelengths are so small, the exit of the pipe begins to resemble a free-field condition, rather than a reactive boundary. Thus, almost no high-frequency energy is reflected back into the pipe, and is primarily found in the beginning of the transient signal radiated out to the far-field. On the other hand, the low-frequency energy is kept in the pipe longer due to the approximate pressure-release boundary condition at the pipe exit. Lower frequencies continue to

ring due to the high amount of energy reflected back down the pipe, radiating (or losing) only a small amount of its energy to the far field after each wavefront impinges on the boundary of the pipe exit. Temporal movement of audible frequencies will largely depend on the geometry of the system, the excitation signal produced, and placement of the receiver.

As noted earlier, Fig. 3 shows the propagation of a single-cycle sine wave with a plane-wave spatial profile. The cutoff frequency corresponding to this profile is $f_0 = 0$ Hz. Therefore, the phase and group speeds are c_0 , and all the energy imparted from the original excitation moves through the pipe undisturbed and in the same form as initially produced. As a result, the pulse-like shape created at the beginning of the pipe is maintained throughout the first propagation down the pipe, from the source to the pipe exit. The pressure profile for the plane-wave mode does not appear as a gated sine wave because this temporal profile was assigned to the acceleration. The pressure profile can be derived analytically (in this case) by interpreting the impedance relation for a plane wave as follows:

$$\begin{aligned}
 p &= \rho_0 c_0 u \\
 &= \rho_0 c_0 \int_0^t \hat{a}(r, \bar{t}) d\bar{t} \\
 &= \frac{\rho_0 c_0 T_d}{2\pi} J_0(\chi_{0,0} r) \left[1 - \cos\left(\frac{2\pi t}{T_d}\right) \right].
 \end{aligned} \tag{28}$$

Thus, only a compression from the plane-wave mode is expected.

The results of Fig. 4 may also be explained through the concepts of group and phase velocity. The cutoff frequency for the first axisymmetric cross mode is approximately 11 kHz. Therefore, frequencies below the cutoff decay exponentially and frequencies above the cutoff propagate without appreciable decay. As seen from the theory, the higher frequencies lead lower frequencies, as their group speeds are higher and therefore must travel through the pipe more quickly. As frequencies increase, their group speeds approach c_0 . However, since the simulation cannot represent many of these higher frequencies because of the finite spatial grid, very little energy is physically given to those frequencies and may therefore be neglected. Additionally, because the boundary condition for the pipe walls is completely rigid, no energy is lost in the associated reflections. The reflections present in higher-order modal propagation would be less significant if the boundary condition included a finite amount of absorption.

As previously noted, a main point of analysis for each simulation was to record the radiated pressure over time as it arrived at the absorbing boundary C_2 of the physical domain depicted in Fig. 2. Figure 5 shows the results of the pressure amplitude as a function of angle and time. The various subplots depict the temporal evolution of the directional radiation due to various pipe modes. One can note the different arrival times for each independently excited mode. The plane-wave mode travels at the sound speed of the fluid c_0 . Assuming $c_0 = 343$ m/s and the sound must travel 1.008 m, the signal should first arrive at the boundary at approximately 2.94 ms. Very high frequencies of higher-order

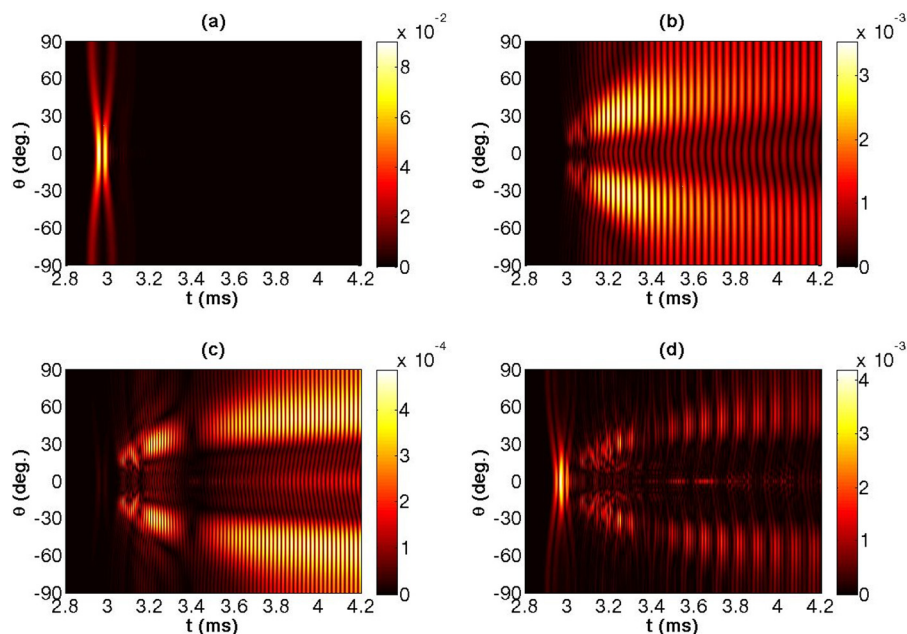


FIG. 5. (Color online) Far-field radiation (pressure magnitude) measured at 0.508 m from the exit of the pipe as a function of angle and time for various modes of the 16 kHz gated sine wave. (a) (0,0) mode. (b) (0,1) mode. (c) (0,2) mode. (d) Combination of several modes, where the spatial component of the normal acceleration is given as $\cos(3\pi r/a)$.

modes can travel close to the sound speed of the fluid; however, the numerical grid must be very fine to account for these frequencies. The main body of energy is contained in frequencies centered at 16 kHz (the frequency of the single-cycle excitation period), which travels notably slower than the plane-wave mode. When multiple modes and frequencies are excited [see Fig. 5(d)], the temporal radiation signal shows arrival of the plane-wave mode first, while each higher-order mode arrives at the absorbing boundary at progressively later times.

V. DISCUSSION

As Stepanishen and Tougas found, the results in Fig. 5 show significant off-axis radiation for higher-order modes.¹⁵ The radiation pattern for a transient signal depends not only on frequency, but also on the spatial profile of the excitation source. More specifically, as either frequency or the pipe mode increases, so does the angle of maximum radiation. Of course, this is with exception to the plane-wave mode whose maximum radiation is *always* on axis. Table I summarizes the angles at which maximum radiation occurs for 8 kHz and 16 kHz single-cycle sine-wave excitation signals.

General features of these simulations, such as the angles at which maximum pressure radiation occur, agree visually with the results obtained by Stepanishen and Tougas. However, the simulations here also include a small amount of on-axis radiation. We remind the reader of the governing assumption in the semi-analytical calculations made by

Stepanishen and Tougas: there is no modal coupling at the pipe exit. Figure 3 shows visible coupling between the impinging plane-wave mode and the first higher-order mode. One can note the apparent presence of the first cross mode in Fig. 3(f) between 0 and -0.2 m. While most of the reflected energy propagates as a plane wave, trailing this wave front is radiation in other higher-order modes—predominantly the first. Because the color scales were clipped considerably to focus on the modal coupling, the sinusoidal pulse appears to be constant in amplitude. Figure 4 is much harder to interpret as energy is continuously moving up and down in the pipe. However, a feel for the coupling is given by analyzing the far-field radiation from this signal, as shown in Fig. 5. Contrary to the work of Stepanishen and Tougas, the energy radiated on axis is non-zero, though small at times. For instance, consider the pressure radiated from the pipe due to excitation of the (0,1) pipe mode [see Fig. 5(b) or Fig. 6(a)]. When considering individual wavefronts in the radiated field, the maximum off-axis pressure is about four times larger than the on-axis pressure (at $t \approx 3.2$ ms) and less than double the on-axis pressure less than a millisecond later.

Though not presented in detail here, these simulations were also confirmed in COMSOL, a commercial finite-element software package. Figure 6 shows a side by side comparison of the radiation as a function of time from the numerical simulation introduced here [Fig. 6(a)] and from COMSOL [Fig. 6(b)]. Agreement between the two simulations regarding the amount of on-axis radiation relative to the peak off-axis radiation for a given wavefront was within 1%. The angles of maximum off-axis radiation also agree to within a fraction of a degree. These simulations mapped the domain using a free-triangular mesh with approximately the same number of elements as the FDM presented here (with the pressure defined using quadratic shape functions), but with only 10 points per wavelength at the 16 kHz center frequency. COMSOL simulations also verified a significant decrease in on-axis radiation for the case involving no pipe

TABLE I. Angles of maximum pressure radiation for the first three modes of the pipe.

	8 kHz	16 kHz
Mode (0,0)	0°	0°
Mode (0,1)	27°	33°
Mode (0,2)	36°	34°

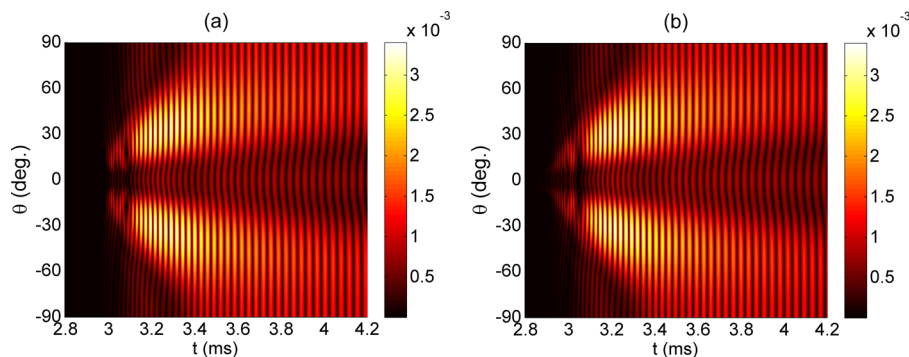


FIG. 6. (Color online) Far-field radiation (pressure magnitude) measured at 0.508 m from the exit of the pipe as a function of angle and time for the (0,1) mode of the 16 kHz gated sine wave. (a) Finite difference simulation result [same as Fig. 5(b)]. (b) COMSOL simulation result.

(an infinitely baffled piston). In this latter result, the on-axis pressure was more than one order of magnitude below the maximum off-axis pressure observed for the same wavefront. It is interesting to note that the computation time for the COMSOL simulation—even with a nearly identical number of elements—took around four times longer to compute. We also note that the COMSOL result in Fig. 6(b) appears to suffer from some minor numerical dispersion artifacts since some radiation at the far boundary exists prior to 2.95 ms (the time at which the earliest possible radiation could arrive). However, this was sufficiently corrected by increasing the number of elements to approximately 850 000 elements, more than four times the original number of elements. While this refined COMSOL simulation greatly reduced the numerical dispersion at the beginning of the pulse, the main body of the signal ($t > 3.1$ ms) was identical to both the results from the COMSOL model and the FDM presented here. A larger number of elements required in the COMSOL model is likely due to the free-triangular mesh used for the simulation; this mapping provided a lower amount of elements per wavelength in the direction of wave propagation, thus admitting problems with numerical dispersion sooner.

Although the numerical simulation presented here eliminates the problem of matching the pipe domain with the half-space domain, the FDM has some issues of its own. First, as mentioned earlier, numerical dispersion requires the simulation to have a sufficiently fine grid for all higher frequencies that are excited within the model. The FDM also deals with an imperfect absorbing boundary, which to a small degree reflects spurious numerical error back into the computational domain. To ensure that the recorded radiation patterns were not significantly affected by the imperfect boundary condition, the boundary was moved farther from the pipe exit (by increasing R) while radiated pressure was recorded at the original distance. Results were the same within numerical error, showing that the presence of the on-axis radiation was not due to the imperfect boundary condition.

VI. CONCLUSIONS

The relatively new numerical method discussed in this paper employs an analytical mapping to an arbitrary domain from a simple rectangular grid in curvilinear coordinates. Relevant analysis to incorporate this method into numerical time-domain simulations was also presented.

This finite-difference method incorporates fully automatic grid control functions for mesh generation that have been shown to exceed grid performance of conventional methods when the geometry contains sharp discontinuities. It was used here to study a rigidly baffled, finite-length pipe and observe coupling of pipe modes between incident and reflected pressure waves and subsequent far-field pressure radiation patterns. Natural modes of the pipe were excited individually by using a Bessel function for the spatial velocity profile. The temporal acceleration used for boundary excitation was a single-cycle sine wave. Each of the signals were varied spatially to excite the (0,0) and (0,1) natural modes of the cylindrical pipe. The independent excitation of modes resulted in unique radiation patterns over time and angle. Results were presented for a single-cycle sine wave at 16 kHz.

Pressures were recorded over angle at the absorptive field boundary, and their peak locations were observed to coincide with those found by Stepanishen and Tougas.¹⁵ From this standpoint, it appears that the models are in agreement. However, the numerical simulations presented here produced a degree of on-axis radiation for higher-order modes, a feature not observed in their model. Simulations performed in COMSOL also confirmed the amount of on-axis radiation seen in the simulations presented here. The difference with the work of Stepanishen and Tougas was likely due to the simplified boundary condition at their pipe exit, in which no coupling between pipe modes was permitted. Excitation of a single mode within the pipe excites many other pipe modes, to varying degrees, upon reflection at the pipe exit. Because the present model requires no boundary condition at this interface, the coupling between the initial pipe modes and *all* other pipe modes (within the limits of grid resolution) are excited upon reflection and may be observed.

Further work may include extending these results to horns (pipes of varying cross-section). The effects seen in the horn may be less pronounced, but a related investigation would help clarify radiation patterns produced by transient signals, which can be much different than their steady-state counterparts. Further work may also include employing a time-dependent, three-dimensional numerical package to excite and study non-axisymmetric modes.

ACKNOWLEDGMENTS

This research has been made possible by funding from Bosch. The authors wish to thank Sebastian Acosta for his

help with, and opinions regarding, the finite-difference models. We thank the Department of Physics and Astronomy at Brigham Young University for the support of author D.R.T., and The University of Texas at Austin for providing access to COMSOL.

- ¹L. Rayleigh, *The Theory of Sound* (Dover Publications, New York, 1945), Vol. 2, pp. 72–74.
- ²J. D. Pearson, “The transient motion of sound waves in tubes,” *Q. J. Mech. Appl. Math.* **6**(3), 313–335 (1953).
- ³J. M. Proud, P. Tamarkin, and E. T. Kornhauser, “Propagation of sound pulses in a dispersive medium,” *J. Acoust. Soc. Am.* **28**(1), 80–85 (1956).
- ⁴K. J. Baumeister, “Influence of exit impedance on finite difference solutions of transient acoustic mode propagation in ducts,” *J. Eng. Indust.* **104**, 113–120 (1982).
- ⁵H. Levine and J. Schwinger, “On the radiation of sound from an unflanged circular pipe,” *Phys. Rev.* **73**(4), 383–406 (1948).
- ⁶Y. Nomura, I. Yamamura, and S. Inawashiro, “On the acoustic radiation from a flanged circular pipe,” *J. Phys. Soc. Jpn.* **15**(3), 510–517 (1960).
- ⁷N. Amir, H. Matzner, and S. Shtrikman, “Acoustics of a flanged cylindrical pipe using singular basis functions,” *J. Acoust. Soc. Am.* **107**(2), 714–724 (2000).
- ⁸K. J. Baumeister, “Numerical techniques in linear duct acoustics—A status report,” *J. Eng. Indust.* **103**(3), 270–281 (1981).
- ⁹A. A. Osipov and I. A. Shirkovskii, “Finite-element calculation of sound fields radiated from the open end of an axisymmetric duct,” *Sov. Phys. Acoust.* **30**(4), 307–310 (1984).
- ¹⁰S. Davis, “Low-dispersion finite difference methods for acoustic waves in a pipe,” *J. Acoust. Soc. Am.* **90**(5), 2775–2781 (1991).
- ¹¹D. W. Quinn, “Finite difference method for computing sound propagation in nonuniform ducts,” *AIAA* **13**(10), 1392–1394 (1975).
- ¹²J. P. Dalmont, C. J. Nederveen, and N. Joly, “Radiation impedance of tubes with different flanges: Numerical and experimental investigations,” *J. Sound Vib.* **244**(3), 505–534 (2001).
- ¹³Y. Tsubakishita, H. Hamana, and T. Yoshikawa, “Finite difference solutions to sound radiation from cylindrical ducts,” *JSME Int. J. Ser. B* **38**(1), 60–65 (1995).
- ¹⁴D. Noreland, “A numerical method for acoustic waves in horns,” *Acta Acust.* **88** 576–586 (2002).
- ¹⁵P. Stepanishen and R. A. Tougas, “Transient acoustic pressure radiated from a finite duct,” *J. Acoust. Soc. Am.* **93**(6), 3074–3084 (1993).
- ¹⁶A. Bayliss and E. Turkel, “Radiation boundary conditions for wave-like equations,” *Commun. Pure Appl. Math.* **33**(6), 707–725 (1980).
- ¹⁷D. Givoli, “Non-reflecting boundary conditions: A review,” *J. Comp. Phys.* **94**, 1–29 (1991).
- ¹⁸D. Givoli, *Numerical Methods for Problems in Infinite Domains* (Elsevier, Amsterdam, 1992), pp. 1–299.
- ¹⁹V. Villamizar and S. Acosta, “Generation of smooth grids with line control for scattering from multiple obstacles,” *Math. Comp. Sim.* **79**(8), 2506–2520 (2009).
- ²⁰A. Winslow, “Numerical solution of the quasilinear poisson equations in a nonuniform triangle mesh,” *J. Comp. Phys.* **1**(2), 149–172 (1966).
- ²¹G. A. Hansen, R. W. Douglass, and A. Zardecki, *Mesh Enhancement* (Imperial College Press, London, 2005), Chap. 8.
- ²²J. F. Thompson, B. K. Soni, and N. G. Weatherill, *Handbook of Grid Generation* (CRC Press, Boca Raton, FL, 1999), Chap. 6.
- ²³V. Villamizar and S. Acosta, “Elliptic grids with nearly uniform cell area and line spacing,” *Electron. Trans. Numer. Anal.* **34**, 59–75 (2009).
- ²⁴S. Acosta and V. Villamizar, “Finite difference on grids with nearly uniform cell area and line spacing for the wave equation on complex domains,” *J. Comp. Appl. Math.* **234**, 1970–1979 (2010).
- ²⁵S. Acosta and V. Villamizar, “Coupling of Dirichlet-to-Neumann boundary condition and finite difference methods in curvilinear coordinates for multiple scattering,” *J. Comp. Phys.* **229**(15), 5498–5517 (2010).
- ²⁶This parameter was calculated by recording the maximum of the outward-propagating signal, and then comparing it to the maximum of the reflected, inward-propagating signal at the same locations. This test was performed at several different locations. Determining the maximum of the reflected signal was possible because the initial signal was so short and thus did not interfere.
- ²⁷D. Blackstock, *Fundamentals of Physical Acoustics* (John Wiley and Sons, New York, 2000), pp. 393, 420–432.
- ²⁸V. Villamizar and M. Weber, “Boundary-conforming coordinates with grid line control for acoustic scattering from complexly shaped obstacles,” *Num. Meth. Part. Diff. Eqs.* **23**(6), 1445–1467 (2007).
- ²⁹L. E. Kinsler, A. R. Frey, A. B. Coppens, and J. V. Sanders, *Fundamentals of Acoustics*, 4th ed. (John Wiley and Sons, New York, 2000), pp. 252–255.